inorganics

MDPI

Article

Construction of $Zn_{0.5}Cd_{0.5}S/Bi_4O_5Br_2$ Heterojunction for Enhanced Photocatalytic Degradation of Tetracycline Hydrochloride

Lan Luo [1], Juan Shen [1,2,*] and Bo Jin [2]

[1] School of Materials and Chemistry, Southwest University of Science and Technology, Mianyang 621010, China; taytay1105@163.com

[2] State Key Laboratory of Environmental-Friendly Energy Materials, Southwest University of Science and Technology, Mianyang 621010, China; jinbo0428@163.com

* Correspondence: sj-shenjuan@163.com; Tel./Fax: +86-816-2419201

Abstract: The development of efficient catalysts with visible light response for the removal of pollutants in an aqueous environment has been a hotspot in the field of photocatalysis research. A $Zn_{0.5}Cd_{0.5}S$ (ZCS) nanoparticle/$Bi_4O_5Br_2$ ultra-thin nanosheet heterojunction was constructed by ultrasound-assisted solvothermal method. The morphology, structure, and optoelectronic properties of the composite were characterized by scanning electron microscopy, X-ray diffraction, X-ray photoelectron spectroscopy, and UV–vis diffuse reflectance spectra. Under simulated visible light illumination, the photocatalytic performance was evaluated through degradation of tetracycline hydrochloride. Results show that the degradation effect by the optimum ZCS/$Bi_4O_5Br_2$ catalyst is superior to pure materials with the kinetic constant that is 1.7 and 9.6 times higher than those of $Bi_4O_5Br_2$ and ZCS, and also has better stability and reusability. Trapping experiments and electron paramagnetic resonance tests find that free radicals in the photocatalytic system are superoxide radicals and holes. This work provides a referable idea for the development of more efficient and recyclable photocatalysts.

Keywords: zinc cadmium sulfide; $Bi_4O_5Br_2$; degradation; heterojunction; tetracycline hydrochloride

Citation: Luo, L.; Shen, J.; Jin, B. Construction of $Zn_{0.5}Cd_{0.5}S/Bi_4O_5Br_2$ Heterojunction for Enhanced Photocatalytic Degradation of Tetracycline Hydrochloride. *Inorganics* **2024**, *12*, 127. https://doi.org/10.3390/inorganics12050127

Academic Editor: Antonino Gulino

Received: 23 March 2024
Revised: 16 April 2024
Accepted: 19 April 2024
Published: 24 April 2024

1. Introduction

Tetracycline hydrochloride (TCH) is widely used in medicine and agriculture as a broad-spectrum antibiotic. It is stable and difficult to degrade naturally, and its overuse poses a serious threat to the environment and human beings [1,2]. The increasing amounts of various types of organic dyes discharged from industrial wastewater also pose a great challenge for water purification [3]. Conventional treatment technologies have difficulty removing pollutants in an efficient and environmentally friendly manner. In recent years, photocatalytic technology has emerged as a potential strategy for degrading hazardous pollutants [4,5]. Semiconductor photocatalytic materials have a strong redox capacity and are capable of converting most organic pollutants into H_2O, CO_2, and other small inorganic molecules for purifying harmful substances. Therefore, developing a new efficient photocatalyst is particularly important.

Bismuth oxyhalide BiOX (X = Cl, Br, I) materials have become a research hotspot in the field of photocatalysis due to their unique layered structure and superior photocatalytic performance [6]. However, their positive conduction band position (CB) and poor carrier separation ability limit the practical applications [7]. Density-functional-transfer (DFT) calculations of BiOBr show that its valence band is hybridized by O 2p and Br 4p orbitals, and the conduction band consists of Bi 6p orbitals; thus, its energy band position and band gap width can be changed by adjusting the ratio of Bi, O, and Br [8]. $Bi_4O_5Br_2$ constructed by this bismuth-rich strategy retains the 2D layered structure of BiOBr but has a narrower

band gap, stronger photogenerated carrier separation efficiency, and better photocatalytic performance [9,10]. However, the photocatalytic role of pure $Bi_4O_5Br_2$ is limited, with low visible light utilization efficiency and high complexation rate of a photogenerated electron–hole pair [11,12]. Therefore, modifications are needed to improve the catalytic activity, including changing the morphology [13], constructing heterojunctions [14–16], doping [17,18], and introducing surface defects [19,20]. Selecting ideal semiconductors with suitable energy band structure to construct heterojunctions with excellent photocatalytic performance is of great significance. For example, Zhang et al. constructed $In_2O_3/Bi_4O_5Br_2$ S-scheme heterojunctions with interfacial oxygen vacancies using a hydrothermal and chemical precipitation method. The obtained catalyst was capable of degrading tetracycline efficiently [21]. Qian et al. synthesized a 2D/2D $Bi_4O_5Br_2/Bi_2WO_6$ Z-scheme heterojunction by chemical co-precipitation and hydrothermal method, which was effective for the stable removal of ciprofloxacin [22]. Therefore, rationally designing heterojunction materials is an effective strategy for improving the photocatalytic activity of $Bi_4O_5Br_2$ while preserving the redox capacity.

In recent years, $Zn_xCd_{1-x}S$ solid solution with excellent photocatalytic properties has been recognized as a promising semiconductor material. One of the highlights is that its forbidden bandwidth and optical response range can be flexibly tuned by varying the molar ratio of Zn^{2+} and Cd^{2+} [23]. Among the series of zinc cadmium sulfide solid solutions, ZCS has been the most extensively researched and widely used for photocatalytic hydrogen precipitation [24,25], degradation of pollutants [26,27], and carbon dioxide reduction [28]. However, pure ZCS has some limitations, such as low efficiency of photogenerated electron–hole pair separation and photocorrosion [29]. These defects can be compensated by constructing heterojunctions with other semiconductors to improve the photocatalytic activity.

Herein, a series of ZCS/$Bi_4O_5Br_2$ heterojunctions were constructed by using a facile ultrasound-assisted solvothermal method. The prepared composite catalysts exhibit the following properties: (1) The ZCS/$Bi_4O_5Br_2$ heterojunction forms a built-in electric field and accelerates the transport of photogenerated carriers at the interface. (2) $Bi_4O_5Br_2$ serves as an oxidation semiconductor to capture the holes of ZCS and strengthen the photocatalytic stability, thereby slightly mitigating the photocorrosion of ZCS nanoparticles. The photocatalytic performance of the material was optimized by appropriately adjusting the ratio of ZCS and $Bi_4O_5Br_2$, which showed an obvious removal effect for several pollutants (TCH, OTC, RhB, and MB). The stability and reusability were demonstrated by cycling tests, and possible TCH degradation pathways and mechanistic predictions were suggested.

2. Results and Discussion

2.1. Material Characterization

The samples were characterized by X-ray diffraction (XRD), as displayed in Figure 1. The diffraction peaks at 24.23°, 29.58°, 31.82°, and 45.65° are observed in pure $Bi_4O_5Br_2$, corresponding to the (112), (11-3), (020), and (422) crystal planes of the monoclinic phase (JCPDS No. 37-0699), respectively [30]. The peaks between cubic CdS and ZnS appearing at 27.44°, 45.49°, and 53.67° belong to the (111), (220), and (311) crystallographic planes of ZCS, respectively, which indicates the successful synthesis of ZCS [31,32]. The main diffraction peaks of as-prepared ZCS/$Bi_4O_5Br_2$ composites clearly correspond to $Bi_4O_5Br_2$ and ZCS without the appearance of other impurity peaks. With the gradual introduction of ZCS, the peak intensity of ZCS in the composite catalysts was strengthened, while the crystal surface strength of $Bi_4O_5Br_2$ was weakened and then increased. This represented the gradual loading of ZCS to $Bi_4O_5Br_2$, and the materials were successfully composited.

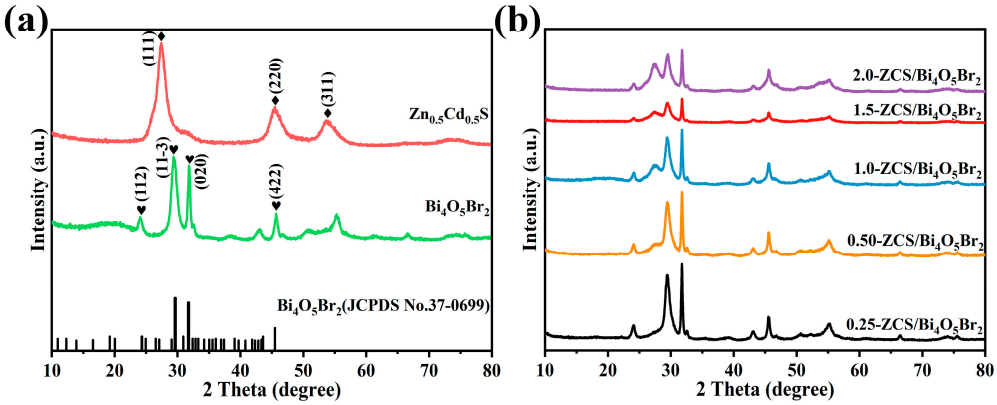

Figure 1. XRD patterns of (**a**) ZCS, $Bi_4O_5Br_2$, and (**b**) ZCS/$Bi_4O_5Br_2$ composites.

The microscopic morphology and structure of ZCS, $Bi_4O_5Br_2$, and ZCS/$Bi_4O_5Br_2$ were observed by scanning electron microscopy (SEM), transmission electron microscopy (TEM), and high-resolution TEM (HRTEM). Figure 2a shows the morphology of ZCS, which consists of small, aggregated nano-microspheres. The pure $Bi_4O_5Br_2$ exhibits irregular stacked nanosheets with relatively smooth surfaces, as shown in Figure 2b. A scanning image of 1.5-ZCS/$Bi_4O_5Br_2$ composite (Figure 2c) shows that ZCS nanoparticles are uniformly loaded on $Bi_4O_5Br_2$ sheet structures, and the surfaces become rough. EDS and elemental mapping images (Figure 3) confirm the uniformly distributed elements of Zn, Cd, S, Bi, Br, and O in 1.5-ZCS/$Bi_4O_5Br_2$.

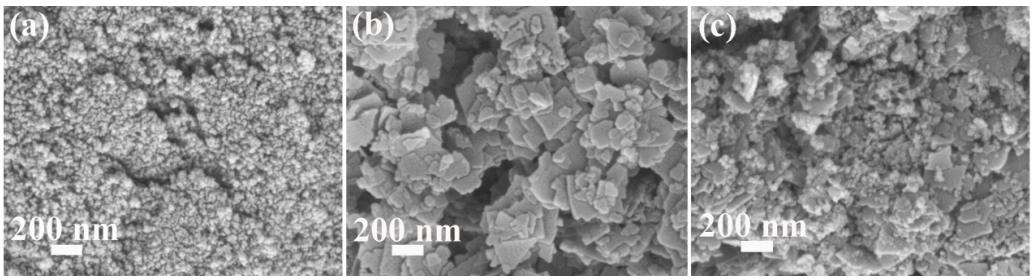

Figure 2. SEM images of (**a**) ZCS, (**b**) $Bi_4O_5Br_2$, and (**c**) 1.5-ZCS/$Bi_4O_5Br_2$.

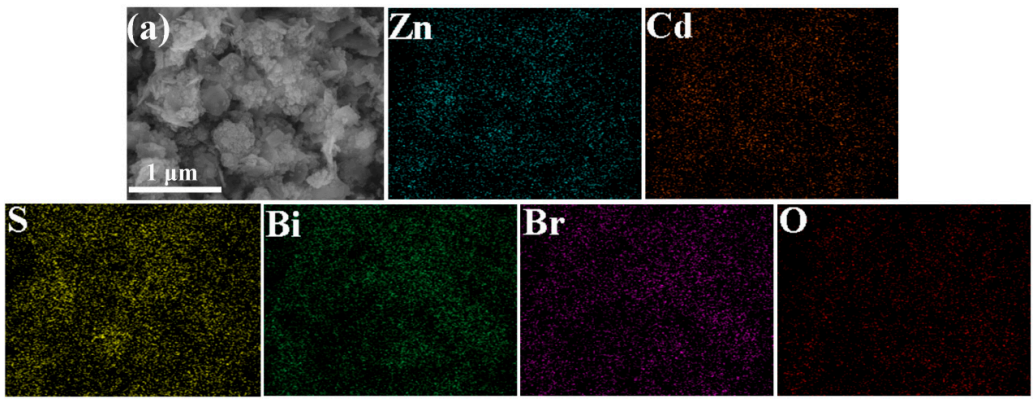

Figure 3. EDS elemental mappings of 1.5-ZCS/$Bi_4O_5Br_2$.

The morphology of nanoparticles and ultra-thin nanosheets was similarly detected in TEM images (Figure 4a), with ZCS nanoparticles dispersed on the surface of $Bi_4O_5Br_2$ nanosheets. The material was further analyzed by HRTEM (Figure 4b,c), the lattice fringes reveal that the lattice spacing of 0.302 nm corresponds to the (11-3) crystal plane of $Bi_4O_5Br_2$, and 0.335 nm matches with the (111) crystal plane of ZCS from the boxed section. The

result is also matched with XRD, further demonstrating the successful synthesis of the ZCS/$Bi_4O_5Br_2$ heterojunction interface.

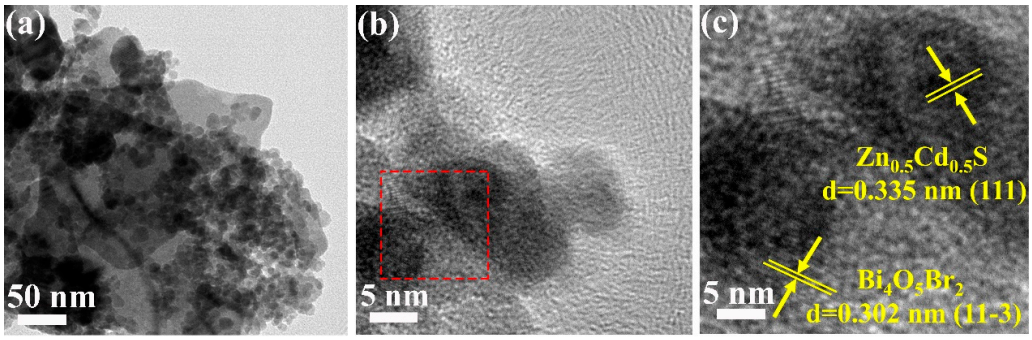

Figure 4. (**a**) TEM and (**b**,**c**) HRTEM images of 1.5-ZCS/$Bi_4O_5Br_2$.

The elemental compositions and valence states were analyzed using X-ray photoelectron spectroscopy (XPS). The full spectrum of 1.5-ZCS/$Bi_4O_5Br_2$ shown in Figure 5a reveals the presence of Bi, O, Br, Zn, Cd, and S. Figure 5b displays that the two characteristic peaks Zn $2p_{1/2}$ and Zn $2p_{3/2}$ of the Zn 2p spectrum in 1.5-ZCS/$Bi_4O_5Br_2$ are attributed to 1044.64 and 1021.61 eV, respectively, proving the presence of Zn^{2+} [33]. The Cd 3d peaks in 1.5-ZCS/$Bi_4O_5Br_2$ at 411.38 and 404.37 eV, belonging to Cd $3d_{3/2}$ and Cd $3d_{5/2}$ of Cd^{2+} (Figure 5c), respectively [34]. In the Bi 4f spectrum shown in Figure 5d, Bi $4f_{5/2}$ and Bi $4f_{7/2}$ are attributed to 163.78 and 158.48 eV, respectively, indicating that Bi element exists in a +3 valence state [11]. Meanwhile, the S 2p peaks of S^{2-} are observed from the spectrum with binding energies at 161.82 and 160.98 eV belonging to S $2p_{1/2}$ and S $2p_{3/2}$, respectively [35]. The result is consistent with the S 2p peaks in pure ZCS. The peaks appearing at 68.80 and 67.80 eV in Figure 5e correspond to Br $3d_{3/2}$ and Br $3d_{5/2}$, respectively, confirming the existence of Br^- [36]. Additionally, the O 1s peaks (Figure 5f) can be fitted to three peaks at 532.25, 530.76, and 529.26 eV related to Bi-O bond and surface-adsorbed oxygen [37]. Compared with pure $Bi_4O_5Br_2$ or ZCS, the binding energies of Bi, Br, and O from 1.5-ZCS/$Bi_4O_5Br_2$ are slightly negatively shifted possibly due to the escape of electrons, and the elements involving Zn, Cd, and S are positively shifted due to the increase of the surrounding electron density, indicating the electronic interaction between $Bi_4O_5Br_2$ and ZCS [38].

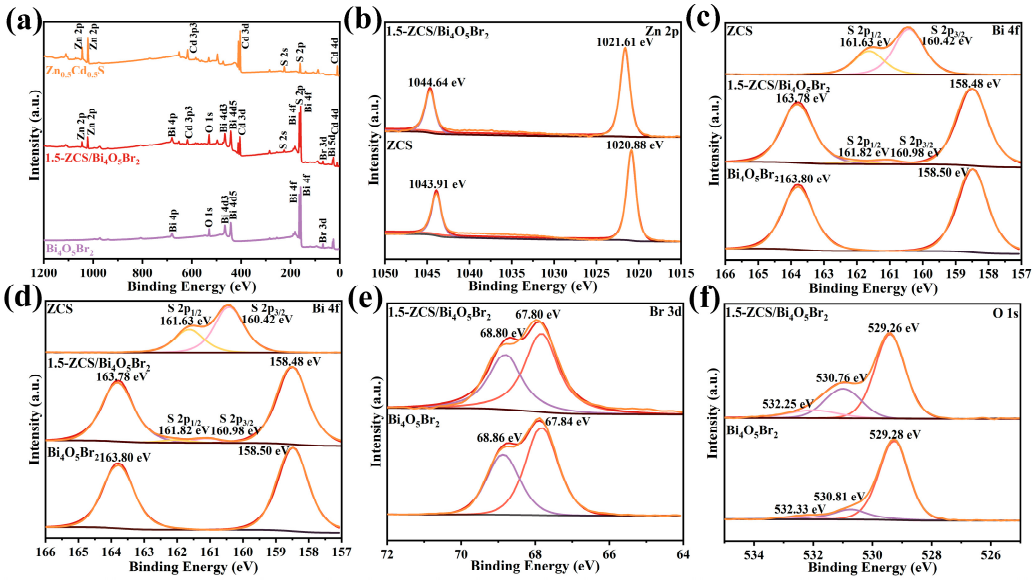

Figure 5. XPS spectra of ZCS, $Bi_4O_5Br_2$, and 1.5-ZCS/$Bi_4O_5Br_2$: (**a**) full spectra, (**b**) Zn 2p, (**c**) Cd 3d, (**d**) Bi 4f, (**e**) Br 3d, and (**f**) O 1s.

The N_2 adsorption–desorption isotherms and pore size distributions of the corresponding samples are presented in Figure 6. The curves of $Bi_4O_5Br_2$ and 1.5-ZCS/$Bi_4O_5Br_2$ are clearly consistent with type IV isotherm, indicating the presence of mesoporous structure of the materials. Evidently, 1.5-ZCS/$Bi_4O_5Br_2$ (68.7 m^2/g, 0.232 cm^3/g) has a higher specific surface area and pore volume than $Bi_4O_5Br_2$ (24.6 m^2/g, 0.167 cm^3/g). The result demonstrates that the introduction of ZCS can significantly increase the specific surface area of $Bi_4O_5Br_2$, thus providing more catalytically active sites with enhanced adsorption capacity and photocatalytic performance.

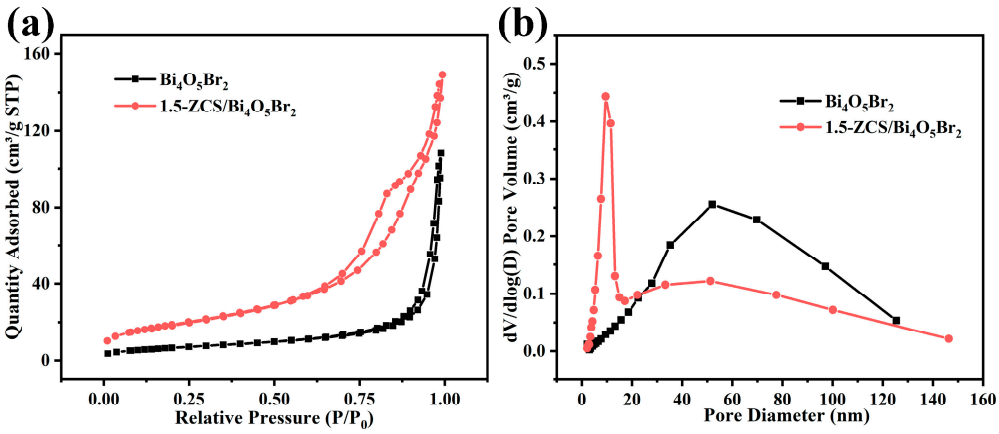

Figure 6. (**a**) N_2 adsorption–desorption isotherms and (**b**) pore size distributions (inset) of $Bi_4O_5Br_2$ and 1.5-ZCS/$Bi_4O_5Br_2$.

2.2. Optoelectronic Properties

The light absorption capacities and energy band structures of ZCS, $Bi_4O_5Br_2$, and ZCS/$Bi_4O_5Br_2$ were revealed by UV–vis diffuse reflectance spectroscopy (DRS). Figure 7a shows the diffuse reflection spectra of the obtained samples in the region of 200–800 nm. The absorption edges of ZCS and $Bi_4O_5Br_2$ are located around 519 and 538 nm, respectively. Compared with pure $Bi_4O_5Br_2$, the composite photocatalysts exhibit enhanced light absorption intensity and a significantly red-shifted characteristic of the absorption edges, indicating that the combination of ZCS and $Bi_4O_5Br_2$ can expand the absorption range of sunlight [39]. Results demonstrates that the effective complexation of ZCS with $Bi_4O_5Br_2$ can improve the absorption capacity and utilization of visible light. The energy bandgap (E_g) values of $Bi_4O_5Br_2$ (2.65 eV) and ZCS (2.43 eV) are calculated in Figure 7b according to the Kubelka–Munk formula [40]:

$$(\alpha hv) = A\left(hv - E_g\right)^{n/2} \quad (1)$$

The bandgap value of 1.5-ZCS/$Bi_4O_5Br_2$ is slightly reduced, which is roughly at 2.38 eV. The narrow band gap made it easier for electrons to jump, and the photocatalytic activity was enhanced. The flat band potential positions −0.49 V (vs. Ag/AgCl) of $Bi_4O_5Br_2$ and −0.88 V (vs. Ag/AgCl) of ZCS are obtained from the tangent intercepts of Mott–Schottky curves, respectively (Figure 7c,d). Converted to standard hydrogen electrode potentials according to the following formula [26]:

$$E_{NHE} = E_{Ag/AgCl} + 0.198 \quad (2)$$

The flat band potentials for $Bi_4O_5Br_2$ and ZCS are −0.29 and −0.68 V (vs. NHE), respectively. The tangent slopes of M–S curves are both positive, indicating that ZCS and $Bi_4O_5Br_2$ are typical n-type semiconductors [41]. For n-type semiconductors, the flat band is generally 0.1 or 0.2 V higher than the conduction band (CB) potential, so the CB positions of $Bi_4O_5Br_2$ and ZCS are −0.49 and −0.88 V (vs. NHE), respectively. Finally, applying the following equation [42]:

$$E_{VB} = E_{CB} + E_g \quad (3)$$

The valence band (VB) potentials of $Bi_4O_5Br_2$ and ZCS are calculated to be 2.16 and 1.55 V, respectively.

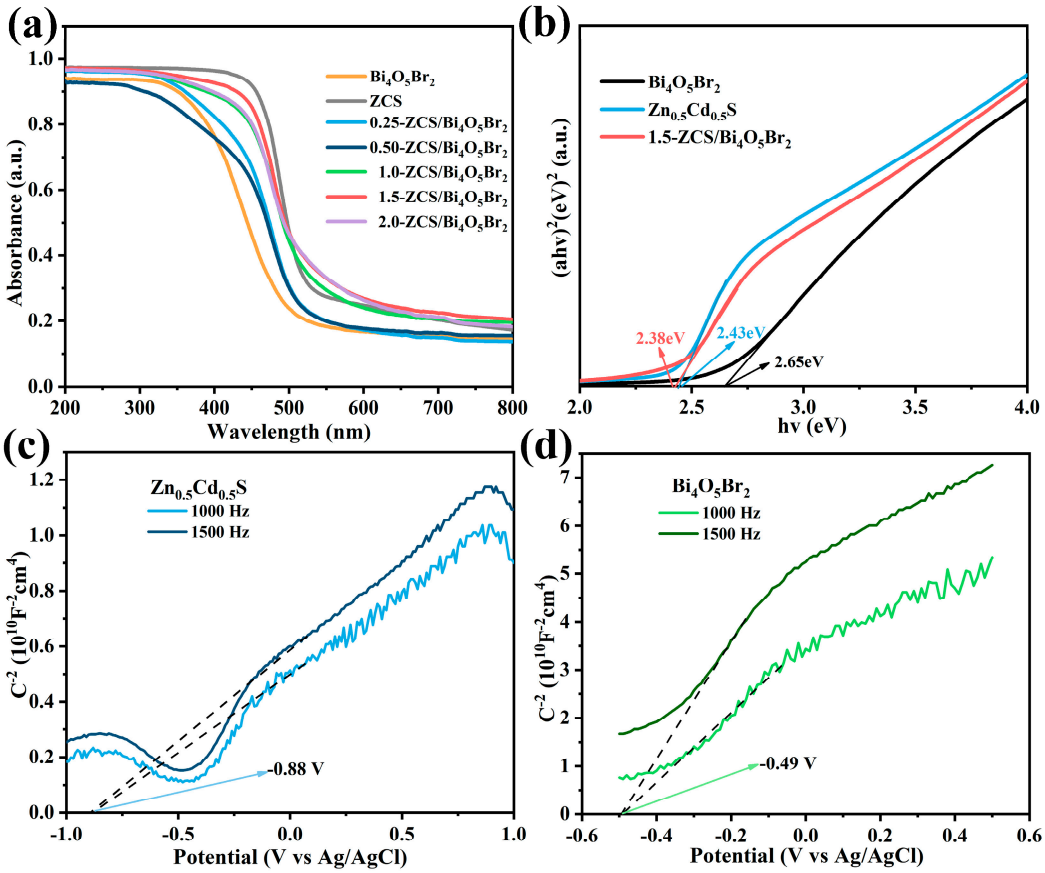

Figure 7. (**a**) UV–vis DRS of obtained samples, (**b**) Tauc plots of $Bi_4O_5Br_2$, ZCS, and 1.5-ZCS/$Bi_4O_5Br_2$, (**c**,**d**) Mott–Schottky plots of ZCS and $Bi_4O_5Br_2$.

The separation efficiency of photogenerated carriers in semiconductors was examined by photoluminescence (PL) spectroscopy. PL spectra of $Bi_4O_5Br_2$, ZCS, and 1.5-ZCS/$Bi_4O_5Br_2$ heterojunction measured at the excitation light wavelength of 325 nm are shown in Figure 8a. The fluorescence intensity of 1.5-ZCS/$Bi_4O_5Br_2$ is weaker than that of uncompounded photocatalysts, illustrating that the possibility of its photogenerated carrier recombination becomes significantly lower [43]. The transfer and separation efficiency of light-induced carriers were further evaluated by impedance tests. Figure 8b displays the electrical impedance spectra (EIS) of $Bi_4O_5Br_2$, ZCS, and 1.5-ZCS/$Bi_4O_5Br_2$ heterojunction. The impedance arc radius of 1.5-ZCS/$Bi_4O_5Br_2$ is obviously smaller than that of ZCS and $Bi_4O_5Br_2$, which suggests that the introduction of ZCS can reduce the resistance of the material. Evidently, ZCS/$Bi_4O_5Br_2$ composite catalysts showed low charge migration resistance and fast electron transport.

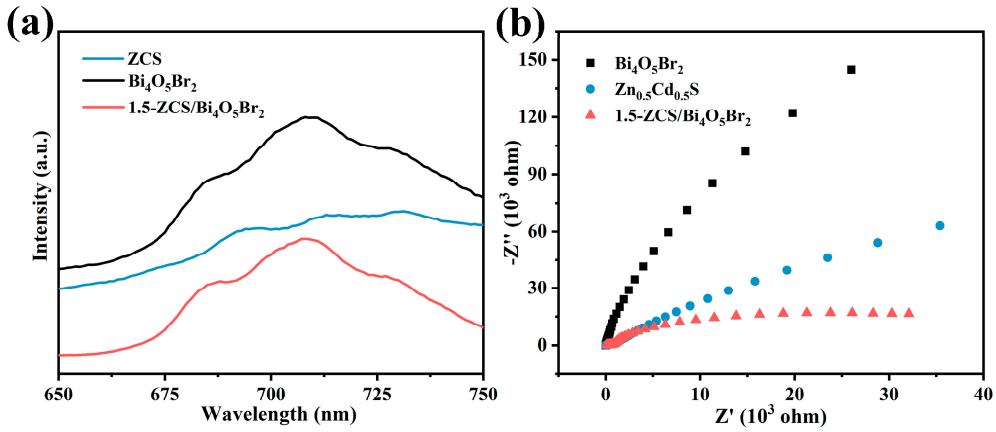

Figure 8. (**a**) PL spectra and (**b**) EIS Nyquist plots of $Bi_4O_5Br_2$, ZCS, and 1.5-ZCS/$Bi_4O_5Br_2$.

2.3. Photocatalytic Performance

The photocatalytic performance of ZCS, $Bi_4O_5Br_2$, and ZCS/$Bi_4O_5Br_2$ was evaluated by degrading TCH. The adsorption–desorption equilibrium experiment was first conducted, as shown in Figure S1. After stirring in the dark for 30 min, the concentration of TCH remains essentially constant, indicating that equilibrium had been reached. In Figure 9a, there is almost no degradation that occurred without the presence of the photocatalyst, proving that TCH is very stable in the natural environment. The degradation rate by pure $Bi_4O_5Br_2$ is 65.8% within 60 min of irradiation, while the degradation rate of ZCS is 14.4%. However, the photocatalytic activity of ZCS/$Bi_4O_5Br_2$ heterojunctions improved significantly. Among them, 1.5-ZCS/$Bi_4O_5Br_2$ shows the highest degradation rate of 84.5%, which is 1.3 and 5.9 times that of $Bi_4O_5Br_2$ and ZCS, respectively. In Figure 9b,c, the removal process of TCH is further analyzed applying the pseudo-first-order kinetic model. It is calculated that 1.5-ZCS/$Bi_4O_5Br_2$ (0.02189 min^{-1}) has the highest apparent rate constant, which is about 1.7 and 9.6 times higher than that of pure $Bi_4O_5Br_2$ (0.01297 min^{-1}) and ZCS (0.00229 min^{-1}), respectively. The above findings corroborate that the effective combination of ZCS and $Bi_4O_5Br_2$ can improve the photocatalytic degradation performance. From the UV–vis absorption spectra (Figure 9d), it can be observed that the intensity of the main characteristic peak of TCH diminishes with time, proving the occurrence of degradation. The reported photocatalytic materials for degrading TCH are displayed in Table 1, and it can be concluded from the comparison that ZCS/$Bi_4O_5Br_2$ catalyst has advantages in degrading TCH. Further, the suitability of 1.5-ZCS/$Bi_4O_5Br_2$ for different pollutants was further investigated. Figure 9e demonstrates that the degradation efficiency of OTC, RhB, and MB can reach 83.3%, 97.7%, and 97.3%, respectively, implying its potential for the removal of contaminants.

Table 1. Comparison of degradation rates of TCH by different catalysts.

Catalyst	Dosage (g/L)	Concentration (mg/L)	Time (min)	Degradation Rate (%)	Reference
PANI/$Bi_4O_5Br_2$	0.4	20	240	85.7	[44]
BiOBr@ZnFe-MOF	0.15	5	90	79.2	[45]
$Bi_4O_5I_2$/$Bi_4O_5Br_2$	0.4	20	120	90.2	[19]
$FeVO_4$/$Bi_4O_5Br_2$	0.5	20	150	88	[46]
$BiOCl_{0.9}I_{0.1}$/β-Bi_2O_3	0.4	20	120	82.4	[47]
$Zn_{0.5}Cd_{0.5}S$/$Bi_4O_5Br_2$	0.4	20	60	84.5	This work

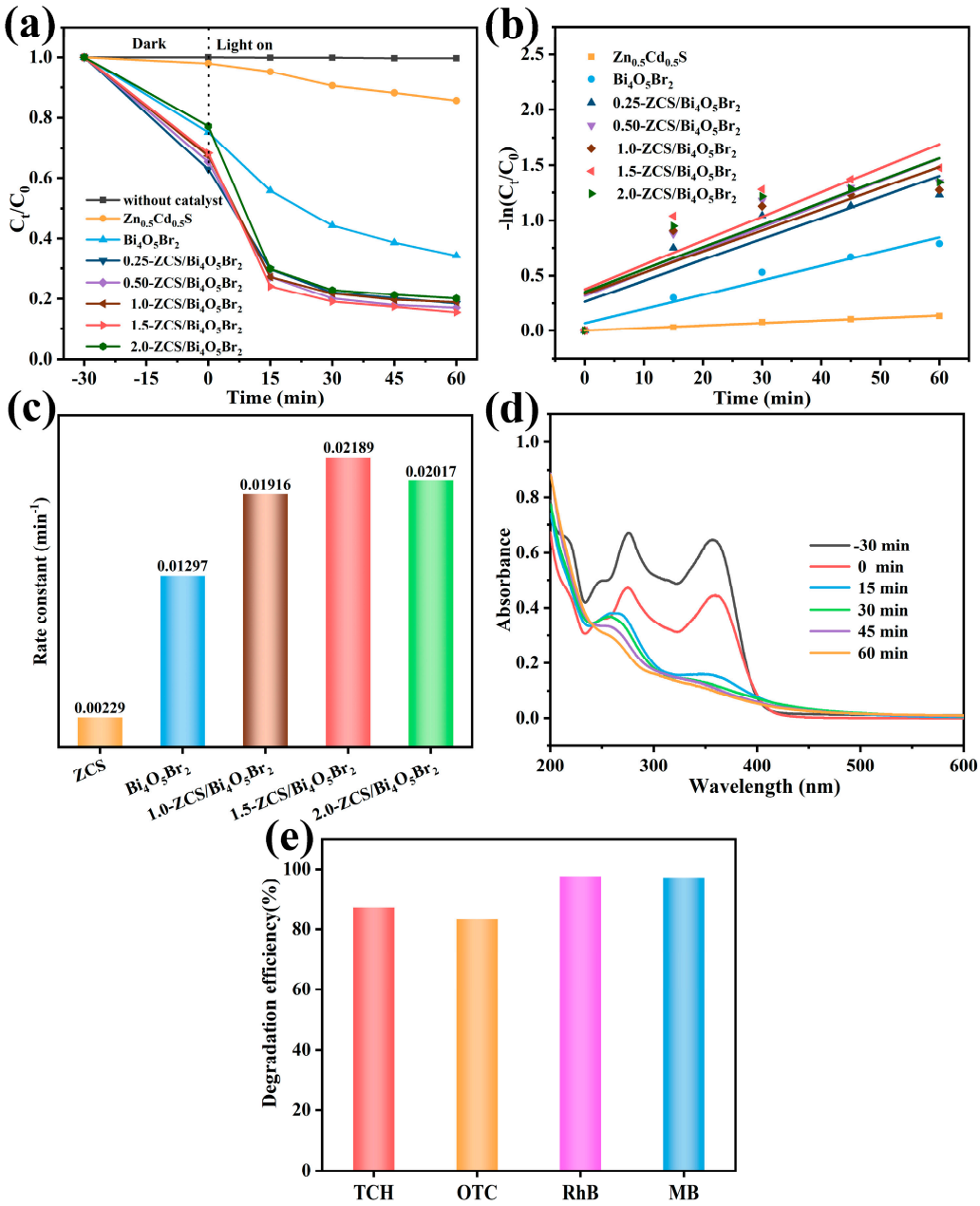

Figure 9. (**a**) Photodegradation efficiencies of TCH by different samples, (**b**) pseudo-first-order degradation kinetics curves, (**c**) apparent rate constants of corresponding catalysts, (**d**) UV–vis spectrum changes of TCH, and (**e**) photodegradation efficiencies of OTC, RhB, and MB.

In practice application, the situation was complex and variable. Thus, the effect of different conditions on the degradation of ZCS/$Bi_4O_5Br_2$ heterojunction was explored, including the initial pH and concentration of TCH solution, as well as the catalyst dosage. As shown in Figure S2a, 1.5-ZCS/$Bi_4O_5Br_2$ catalyst has the best photodegradation ability at a neutral initial pH value, and also maintains favorable TCH removal under different pH gradients, indicating a wider pH application range. Figure S2b shows the removal rate of TCH with different catalyst dosages. The dosage increases from 0.2 to 0.5 g/L, and the degradation rate increases from 78.0% to 86.0%. More pollutants can be adsorbed to the catalyst surface to participate in the photoreaction, and more reactive sites can be provided. The differences in TCH removal effects were not significant when 1.5-ZCS/$Bi_4O_5Br_2$ dosage was 0.4 and 0.5 g/L, respectively. Therefore, 0.4 g/L was the optimal catalyst dosage. Figure S2c shows the degradation efficiency at different TCH concentrations. The

concentrations range from 10 to 40 mg/L, and the degradation rates are 87.3%, 84.5%, 80.2%, and 75.5%, respectively. As the pollutant concentration increased, the removal rate decreased, which was due to the accumulation of substrates and intermediates masking some active sites on the surface of catalyst. And the active radicals produced by a certain amount of catalyst were also limited. Considering the practical application and economic value, 20 mg/L of TCH solution was selected for the following experiments.

The stability and reusability of the photocatalyst are also an important evaluation index. The solution after each round of degradation was filtered off the supernatant, and the catalyst was collected by centrifugation, washed, and dried for the next round of photodegradation experiments. As illustrated in Figure 10a, the photocatalytic activity of 1.5-ZCS/$Bi_4O_5Br_2$ decreases slightly after five cycles of degradation experiments but is still superior to that of the pure ZCS and $Bi_4O_5Br_2$. The result indicates that the catalyst has a long service life. Peak structures of XRD pattern (Figure 10b) before and after cycling remain basically the same, which also demonstrates the stability of its crystalline phase structure.

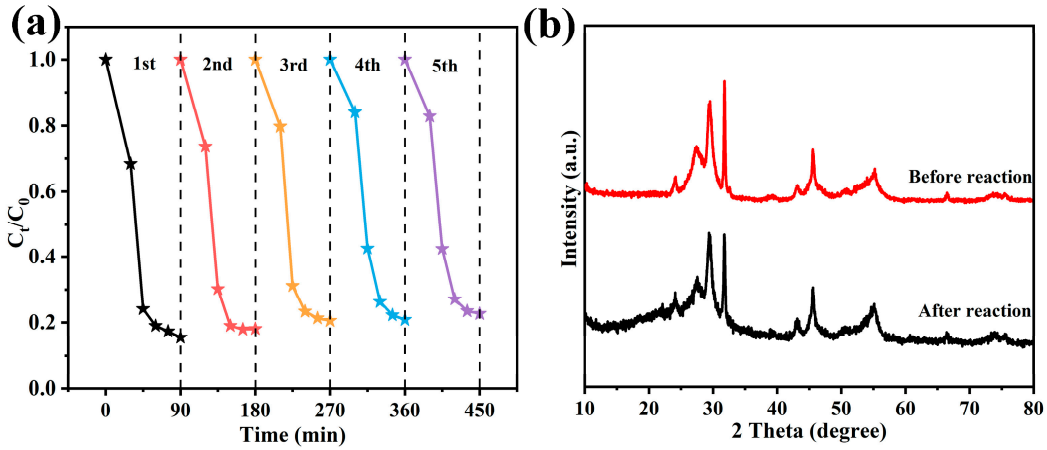

Figure 10. (**a**) Cycling experiments of 1.5-ZCS/$Bi_4O_5Br_2$, (**b**) XRD plots before and after cycling.

2.4. Analysis of Possible Degradation Pathways

The intermediate products in the degradation of TCH were identified using LC-MS. On the basis of the mass spectrometry m/z results (Figure S3), the corresponding intermediates and two possible degradation pathways are deduced. The strong peak at m/z = 445 corresponds to the mass-to-charge ratio of TCH. In pathway I, the introduction of a hydroxyl group produces the intermediate P1 (m/z = 459), followed by N-demethylation and hydroxylation occurring with the detection of P2 (m/z = 417). P2 dissociates to P3 (m/z = 274) via ring-opening and reduction reaction. Furthermore, P2 is dehydrated to produce P4 (m/z = 399) and then degrades to P5 (m/z = 338) by ring-opening, demethylation, and hydroxylation reactions. In pathway II, TCH is degraded to the intermediate P6 (m/z = 391) via deamination reaction and hydroxylation, and then by a ring-opening reaction to produce P7 (m/z = 234), which undergoes a dehydration process and other reactions to produce P8 (m/z = 217). These intermediate substances may be further degraded to obtain smaller masses of organic molecules (P9–P11, m/z = 194, 171, and 114), finally mineralizing to CO_2 and H_2O. The postulated degradation pathways are shown in Figure 11.

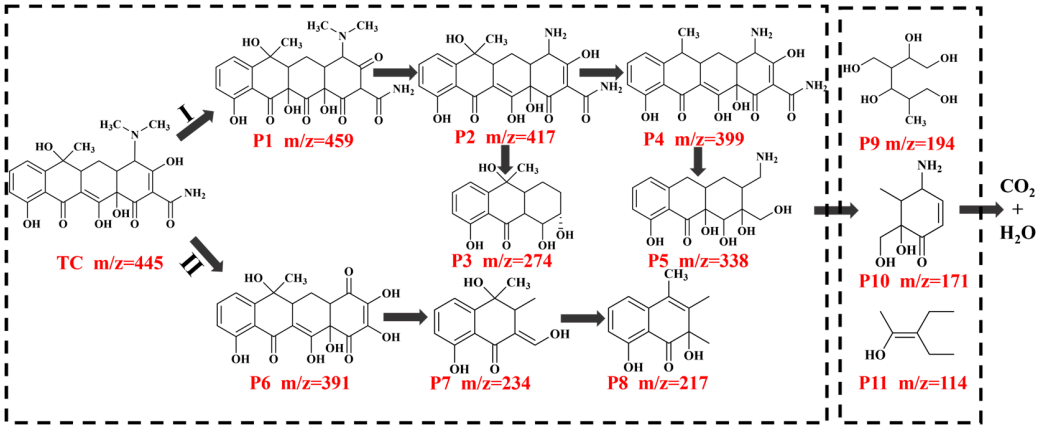

Figure 11. Proposed TCH degradation pathways by 1.5-ZCS/$Bi_4O_5Br_2$.

2.5. Photocatalytic Mechanism

During the photocatalysis process, organic pollutants were degraded through the generation of active species including $\cdot O_2^-$, h^+, and ·OH by the catalysts. Corresponding scavengers such as para-benzoquinone (BQ, $\cdot O_2^-$ scavenger), ethylenediaminetetraacetic acid disodium salt (EDTA-2Na, h^+ scavenger), and isopropanol (IPA, ·OH scavenger) were added during the degradation of TCH to identify the main active substances by trapping experiments. As depicted in Figure 12a, the degradation rates decrease from 84.5% to 44.5% ($\cdot O_2^-$), 61.6% (h^+), and 83.5% (·OH), indicating that $\cdot O_2^-$ and h^+ are the most important active radicals. The EPR tests further confirmed the production of $\cdot O_2^-$ and h^+ in the photocatalytic system. In Figure 12b, the signal of DMPO-$\cdot O_2^-$ could not be recognized under dark condition for 1.5-ZCS/$Bi_4O_5Br_2$. The EPR peak intensity increases after 15 min of light, and the signal is obviously enhanced. The signal generated under dark condition belongs to the capture agent TEMPO, and the intensity of the EPR peak decreases after providing light instead, precisely because the generation of h^+ neutralizes the signal from TEMPO, making the signal weaker (Figure 12c).

The CB and VB positions of ZCS are −0.88 and 1.55 V, while $Bi_4O_5Br_2$ are −0.49 and 2.16 V, respectively. Both semiconductors have more negative potentials and can produce $\cdot O_2^-$ ($O_2/\cdot O_2^-$, −0.33 V vs. NHE) [48]. The redox capacity of $Bi_4O_5Br_2$ enables H_2O molecules to produce ·OH ($H_2O/\cdot OH$, 1.99 V vs. NHE) [49], but ·OH ($OH^-/\cdot OH$, 2.27 V vs. NHE) derived from OH^- cannot be generated [50]. Thus, ·OH had minimal participation in the degradation of TCH, which matched the trapping experimental results. Under visible light excitation, photogenerated electrons and holes were produced in the VB and CB of ZCS and $Bi_4O_5Br_2$, respectively. If the photocatalytic mechanism followed the traditional type II heterojunction transfer theory, $\cdot O_2^-$ would not be generated due to the more positive CB of ZCS than $\cdot O_2^-$ ($O_2/\cdot O_2^-$), and the VB of $Bi_4O_5Br_2$ would be more negative than ·OH ($\cdot OH/H_2O$) or ·OH ($\cdot OH/OH^-$) and unable to produce ·OH, which was contrary to the trapping experiments. Combining the above analyses, the transfer mechanism could be hypothesized in Figure 13. When the two semiconductors contacted closely, the electrons of ZCS spontaneously flowed to $Bi_4O_5Br_2$ until the Fermi energy levels reached equilibrium. Similarly, electron consumption accelerates the transfer of photogenerated holes in the VB of $Bi_4O_5Br_2$ to that of ZCS with a higher potential. At the heterojunction interface, $Bi_4O_5Br_2$ was negatively charged and ZCS was positively charged, thus forming an internal electric field. The recombination of electrons in the CB of $Bi_4O_5Br_2$ and holes in the VB of ZCS under Coulomb force and photoexcitation promoted photogenerated charge separation. Therefore, the soluble oxygen could be reduced to $\cdot O_2^-$ with the presence of photogenerated electrons in the CB of ZCS, and the remaining highly

oxidized h^+ in the VB of $Bi_4O_5Br_2$ was directly involved in the degradation of pollutants. The whole process is summarized as follows:

$$ZCS/Bi_4O_5Br_2 + hv \rightarrow ZCS/Bi_4O_5Br_2(e^-, h^+) \quad (4)$$

$$e^-(Bi_4O_5Br_2) + h^+(ZCS) \rightarrow \text{Recombination} \quad (5)$$

$$e^-(ZCS) + O_2 \rightarrow \cdot O_2^- \quad (6)$$

$$h^+(Bi_4O_5Br_2) + H_2O \rightarrow \cdot OH + h^+ \quad (7)$$

$$\cdot O_2^- + h^+ + \cdot OH + TCH \rightarrow CO_2 + H_2O + \text{Small molecules} \quad (8)$$

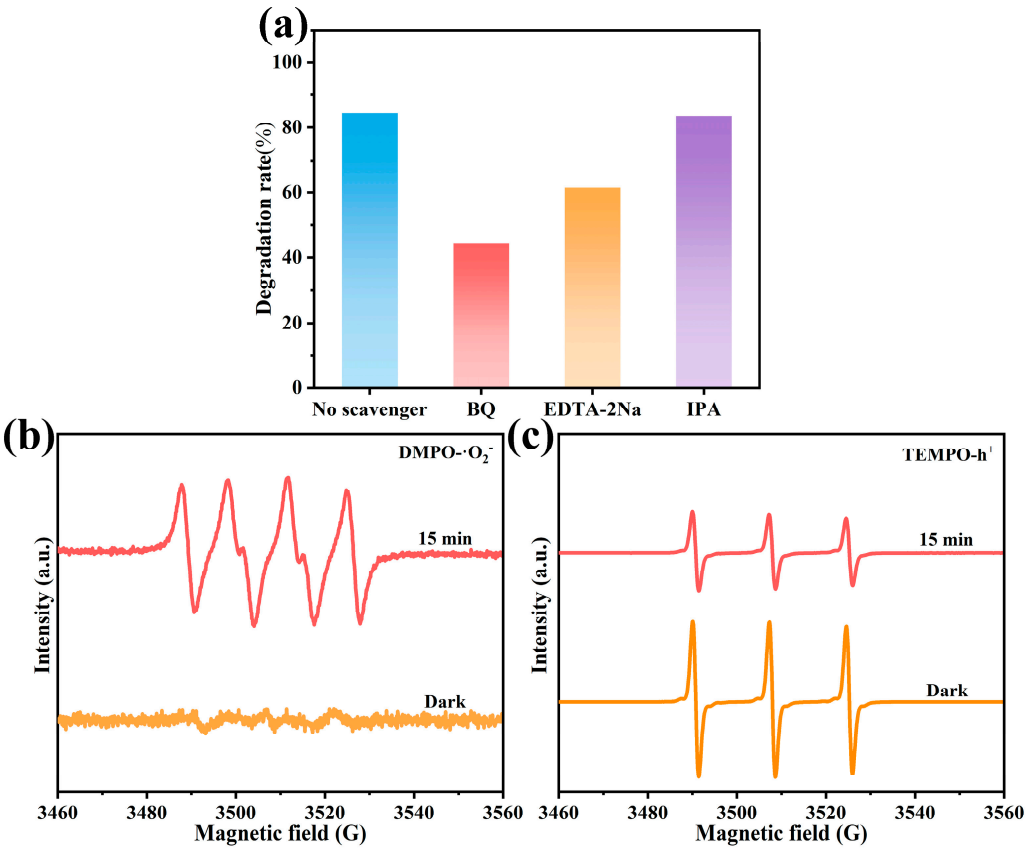

Figure 12. (**a**) Trapping experiments for the photodegradation of TCH with 1.5-ZCS/$Bi_4O_5Br_2$, (**b**,**c**) EPR spectra of DMPO-$\cdot O_2^-$ and TEMPO-h^+.

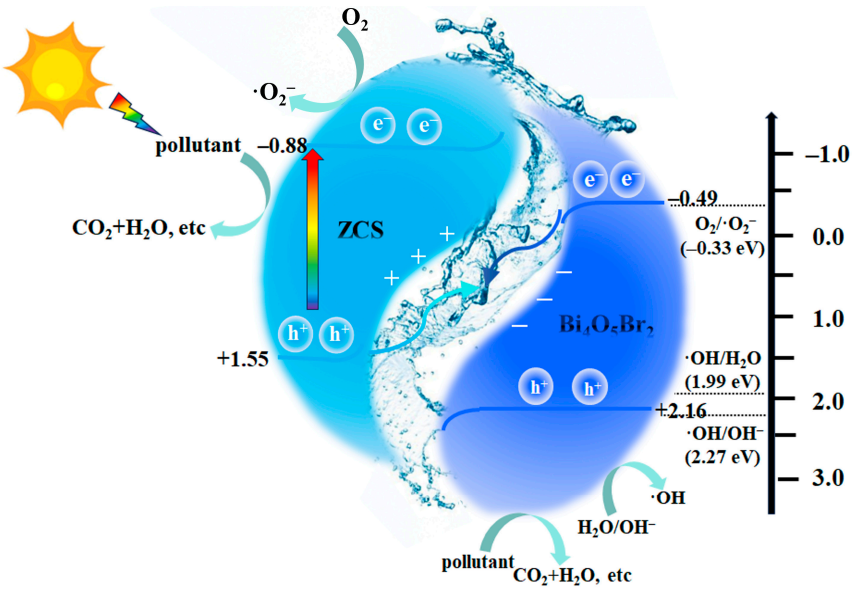

Figure 13. Schematic diagram of possible photocatalytic mechanism.

3. Experimental Section

3.1. Preparation of $Zn_{0.5}Cd_{0.5}S$

$Zn_{0.5}Cd_{0.5}S$ was easily prepared by using the solvothermal method. Quantities of 0.3296 g of $Zn(CH_3COO)_2{\cdot}2H_2O$ and 0.3998 g of $Cd(CH_3COO)_2{\cdot}2H_2O$ were completely dissolved by ultrasonication with 40 mL of ethylene glycol solution, then Na_2S solution was added dropwise according to the molar ratio of Zn: Cd: S = 1: 1: 3 and stirred for 4 h. Next, the mixed solution was poured into a 100 mL Teflon-lined autoclave at 160 °C for 4 h. The sample was washed with ethanol and deionized water repeatedly by centrifugation after natural cooling and dried under vacuum at 60 °C overnight to obtain ZCS nanoparticles.

3.2. Preparation of $Bi_4O_5Br_2$

$Bi_4O_5Br_2$ nanosheets were prepared according to a previous report with minor modifications [51]. Specifically, 0.7277 g of $Bi(NO_3)_3{\cdot}5H_2O$ was added into 15 mL of ethylene glycol solution, and 0.1786 g of KBr was added into 10 mL of deionized water, dissolved by sonication for 0.5 h. Thereafter, the KBr solution was slowly dripped into $Bi(NO_3)_3$ solution, and the white colloid appeared gradually. The pH value was adjusted to about 9 by using dilute ammonia and continued stirring. Finally, the homogeneously mixed solution of $Bi_4O_5Br_2$ precursor was kept at 140 °C for 12 h. The reaction product was washed and dried to obtain milky white $Bi_4O_5Br_2$ powder.

3.3. Preparation of $Zn_{0.5}Cd_{0.5}S/Bi_4O_5Br_2$

A simple ultrasound-assisted solvothermal method was used to synthesize $Zn_{0.5}Cd_{0.5}S/Bi_4O_5Br_2$ composites. A total of 0.1000 g of $Bi_4O_5Br_2$ was dispersed ultrasonically in 20 mL of ethanol to form a homogeneous solution. Next, ZCS was added at the mass ratio X:1 wt.% (X = 0.25, 0.50, 1.0, 1.5, 2.0, which was the mass ratio of ZCS and $Bi_4O_5Br_2$) and sonicated for 1 h, followed by stirring for 2 h. The solutions were transferred into a 50 mL Teflon-lined autoclave, and 100 °C heat was employed for 10 h. After cooling, the composites were washed with ethanol and deionized water to obtain the final substance named X-ZCS/$Bi_4O_5Br_2$ (X = 0.25, 0.50, 1.0, 1.5, 2.0). The whole preparation process is displayed in Scheme 1.

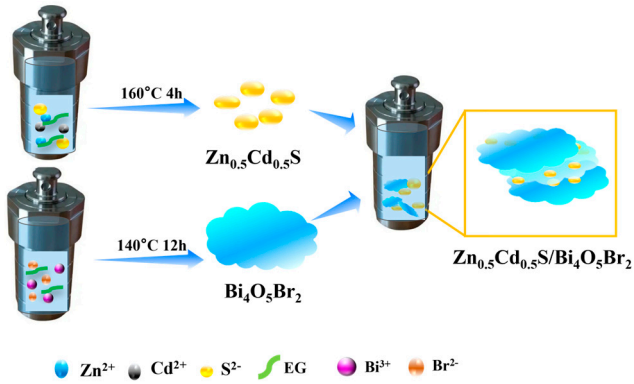

Scheme 1. Schematic illustration of the preparation of ZCS/$Bi_4O_5Br_2$ composites.

3.4. Characterization

Specific characterizations are detailed in the Supplementary Materials.

3.5. Photocatalytic Performance Measurements

The photocatalytic performance was evaluated by using TCH (20 mg/L), OTC, RhB, and MB (10 mg/L) as target pollutants, pH = 7 for all contaminant solutions, and a 300 W xenon lamp as a simulated light source. About 20 mg of catalyst was weighed and dispersed homogeneously into 50 mL of contaminant solution and stirred under dark condition for 0.5 h to reach adsorption–desorption equilibrium. Then, 4 mL of suspension was extracted at 15 min intervals after irradiation and centrifuged to test the maximum absorbance at 357 nm of the obtained supernatant with a Shimadzu UV-1900 spectrophotometer. The degradation rate is calculated via the following equation:

$$\text{Removal rate\%} = (1 - C_t/C_0) \times 100\% \quad (9)$$

where C_0 is the initial concentration of the pollutant solution, and C_t is the concentration at a certain degradation time t (min).

4. Conclusions

In this work, a ZCS/$Bi_4O_5Br_2$ heterojunction was successfully prepared. The better degradation properties of optimized ZCS/$Bi_4O_5Br_2$ were attributed to the formation of an electric field inside the heterojunction, realizing the fast separation of carriers at the interface between ZCS and $Bi_4O_5Br_2$ while also preserving their redox capabilities. Compared with ZCS (14.3%) and $Bi_4O_5Br_2$ (65.8%), 1.5-ZCS/$Bi_4O_5Br_2$ could degrade TCH up to 84.5% and exhibited excellent stability, as indicated by recycling experiments. Here, $\cdot O_2^-$ and h^+ played a dominant role during the elimination process. The suitability for other pollutants' degradation was validated, and the results showed that it also had a better removal effect on OTC (83.3%), RhB (97.7%), and MB (97.3%). Therefore, this study provides a possible strategy for the modification of bismuth-rich materials and the preparation of efficient photocatalysts.

Supplementary Materials: The following supporting information can be downloaded at: https://www.mdpi.com/article/10.3390/inorganics12050127/s1, Figure S1: the adsorption curve of 1.5-ZCS/$Bi_4O_5Br_2$ under dark; Figure S2: effect of (a) initial pH of TCH solution, (b) catalyst dosage, and (c) pollutant concentration; Figure S3: LC-MS spectra of TCH degradation process during different irradiation times: (a) 0 min, (b) 30 min, (c) 60 min. In addition, specific characterization methods are placed in the supplementary materials.

Author Contributions: Conceptualization, methodology, validation, formal analysis, investigation, data curation, visualization and writing—original draft preparation, L.L.; resources, writing—review and editing, supervision, project administration and funding acquisition, J.S. and B.J. All authors have read and agreed to the published version of the manuscript.

Funding: This work was supported by the financial support received from the basic research project of Sichuan Province for Science and Technology Development (No. 2019YJ0355), Outstanding Youth Science and Technology Talents Program of Sichuan Province (No. 19JCQN0085), the Project of State Key Laboratory of Environment-friendly Energy Materials, Southwest University of Science and Technology (project No. 22fksy18).

Data Availability Statement: Data are contained within the article.

Conflicts of Interest: The authors declare no conflict of interest.

References

1. Lu, Z.Y.; Ma, Y.L.; Zhang, J.T.; Fan, N.S.; Huang, B.C.; Jin, R.C. A critical review of antibiotic removal strategies: Performance and mechanisms. *J. Water Process Eng.* **2020**, *38*, 101681. [CrossRef]
2. Yang, J.; Chen, Y.; Xu, P.; Li, Y.; Jia, X.; Song, H. Fabrication of compressible and underwater superoleophobic carbon/g-C_3N_4 aerogel for wastewater purification. *Mater. Lett.* **2019**, *254*, 210–213. [CrossRef]
3. Al-Buriahi, A.K.; Al-Gheethi, A.A.; Kumar, P.S.; Mohamed, R.M.S.R.; Yusof, H.; Alshalif, A.F.; Khalifa, N.A. Elimination of rhodamine B from textile wastewater using nanoparticle photocatalysts: A review for sustainable approaches. *Chemosphere* **2022**, *287*, 132162. [CrossRef]
4. Wang, J.; Zhuan, R. Degradation of antibiotics by advanced oxidation processes: An overview. *Sci. Total Environ.* **2020**, *701*, 135023. [CrossRef]
5. Sharma, K.; Dutta, V.; Sharma, S.; Raizada, P.; Hosseini-Bandegharaei, A.; Thakur, P.; Singh, P. Recent advances in enhanced photocatalytic activity of bismuth oxyhalides for efficient photocatalysis of organic pollutants in water: A review. *J. Ind. Eng. Chem.* **2019**, *78*, 1–20. [CrossRef]
6. Miao, Z.; Wang, Q.; Zhang, Y.; Meng, L.; Wang, X. In situ construction of S-scheme AgBr/BiOBr heterojunction with surface oxygen vacancy for boosting photocatalytic CO_2 reduction with H_2O. Appl. *Catal. B Environ.* **2022**, *301*, 120802. [CrossRef]
7. Rashid, J.; Abbas, A.; Chang, L.C.; Iqbal, A.; Haq, I.U.; Rehman, A.; Awan, S.U.; Arshad, M.; Rafique, M.; Barakat, M.A. Butterfly cluster like lamellar BiOBr/TiO_2 nanocomposite for enhanced sunlight photocatalytic mineralization of aqueous ciprofloxacin. *Sci. Total Environ.* **2019**, *665*, 668–677. [CrossRef]
8. Zang, J.; Chen, C.; Chen, X.; Yang, Y. $Bi_4O_5Br_2$ nanosheets modified by carbon quantum dots: Efficient BPA degradation induced by enhanced absorption and Z-scheme charge transfer. *J. Alloys Compd.* **2023**, *935*, 167988. [CrossRef]
9. Bai, Y.; Chen, T.; Wang, P.; Wang, L.; Ye, L. Bismuth-rich $Bi_4O_5X_2$ (X = Br, and I) nanosheets with dominant {101} facets exposure for photocatalytic H_2 evolution. *Chem. Eng. J.* **2016**, *304*, 454–460. [CrossRef]
10. Mao, D.; Ding, S.; Meng, L.; Dai, Y.; Sun, C.; Yang, S.; He, H. One-pot microemulsion-mediated synthesis of Bi-rich $Bi_4O_5Br_2$ with controllable morphologies and excellent visible-light photocatalytic removal of pollutants. *Appl. Catal. B Environ.* **2017**, *207*, 153–165. [CrossRef]
11. Zhao, X.; You, Y.; Huang, S.; Wu, Y.; Ma, Y.; Zhang, G.; Zhang, Z. Z-scheme photocatalytic production of hydrogen peroxide over $Bi_4O_5Br_2$/g-C_3N_4 heterostructure under visible light. *Appl. Catal. B Environ.* **2020**, *278*, 119251. [CrossRef]
12. Ma, Y.; Qian, X.; Arif, M.; Xia, J.; Fan, H.; Luo, J.; He, G.; Chen, H. Z-scheme $Bi_4O_5Br_2$/MIL-88B(Fe) heterojunction for boosting visible light catalytic oxidation of tetracycline hydrochloride. *Appl. Surf. Sci.* **2023**, *611*, 155667. [CrossRef]
13. Jin, X.; Lv, C.; Zhou, X.; Xie, H.; Sun, S.; Liu, Y.; Meng, Q.; Chen, G. A bismuth rich hollow $Bi_4O_5Br_2$ photocatalyst enables dramatic CO_2 reduction activity. *Nano Energy* **2019**, *64*, 103955. [CrossRef]
14. Chang, F.; Li, S.; Shi, Z.; Qi, Y.; Liu, D.; Liu, X.; Chen, S. Boosted photocatalytic NO removal performance by S-scheme hierarchical composites WO_3/$Bi_4O_5Br_2$ prepared through a facile ball-milling protocol. *Sep. Purif. Technol.* **2021**, *278*, 119662. [CrossRef]
15. Chang, F.; Yan, W.; Wang, X.; Peng, S.; Li, S.; Hu, X. Strengthened photocatalytic removal of bisphenol a by robust 3D hierarchical n-p heterojunctions $Bi_4O_5Br_2$-MnO_2 via boosting oxidative radicals generation. *Chem. Eng. J.* **2022**, *428*, 131223. [CrossRef]
16. Chen, Y.; Zhao, C.; Ma, S.; Xing, P.; Hu, X.; Wu, Y.; He, Y. Fabrication of a Z-scheme AgBr/$Bi_4O_5Br_2$ nanocomposite and its high efficiency in photocatalytic N_2 fixation and dye degradation. *Inorg. Chem. Front.* **2019**, *6*, 3083–3092. [CrossRef]
17. Weng, P.; Cai, Q.; Wu, H.; Zhang, L.; Wu, K.; Guo, J. Facile synthesis of flower-like CQDs/S-$Bi_4O_5Br_2$ composites as a highly efficient visible-light response photocatalyst for ciprofloxacin degradation. *J. Mater. Sci.* **2022**, *57*, 1977–1993. [CrossRef]
18. Wu, D.; Wu, C.; Tan, H. Facile synthesis of novel I-doped $Bi_4O_5Br_2$ nanosheets with enhanced visible light photocatalytic activity. *J. Mater. Sci. Mater. Electron.* **2018**, *29*, 11090–11095. [CrossRef]
19. Jia, X.; Shen, Z.; Han, Q.; Bi, H. Rod-like $Bi_4O_5I_2$/$Bi_4O_5Br_2$ step-scheme heterostructure with oxygen vacancies synthesized by calcining the solid solution containing organic group. *Chin. J. Catal.* **2022**, *43*, 288–302. [CrossRef]
20. Li, P.; Cao, W.; Zhu, Y.; Teng, Q.; Peng, L.; Jiang, C.; Feng, C.; Wang, Y. NaOH-induced formation of 3D flower-sphere BiOBr/$Bi_4O_5Br_2$ with proper-oxygen vacancies via in-situ self-template phase transformation method for antibiotic photodegradation. *Sci. Total Environ.* **2020**, *715*, 136809. [CrossRef]
21. Zhang, X.; Zha, X.; Luo, Y.; Liu, T.; Chen, G.; He, X. In_2O_3 Nanoparticle/$Bi_4O_5Br_2$ Nanosheet S-Scheme Heterojunctions with Interfacial Oxygen Vacancies for Photocatalytic Degradation of Tetracycline. *ACS Appl. Nano Mater.* **2023**, *6*, 11877–11887. [CrossRef]

22. Qian, X.; Ma, Y.; Arif, M.; Xia, J.; He, G.; Chen, H. Construction of 2D/2D $Bi_4O_5Br_2/Bi_2WO_6$ Z-scheme heterojunction for highly efficient photodegradation of ciprofloxacin under visible light. *Sep. Purif. Technol.* **2023**, *316*, 123794. [CrossRef]
23. Li, Y.; Sun, B.; Lin, H.; Ruan, Q.; Geng, Y.; Liu, J.; Wang, H.; Yang, Y.; Wang, L.; Tam, K.C. Efficient visible-light induced H_2 evolution from T-$Cd_xZn_{1-x}S$/defective MoS_2 nano-hybrid with both bulk twinning homojunctions and interfacial heterostructures. *Appl. Catal. B Environ.* **2020**, *267*, 118702. [CrossRef]
24. Song, J.; Sun, R.; Chen, Y.; Sun, D.; Li, X. l-Cysteine assisted synthesis of $Zn_{0.5}Cd_{0.5}S$ solid solution with different morphology, crystal structure and performance for H_2 evolution. *Int. J. Hydrogen Energy* **2018**, *43*, 18220–18231. [CrossRef]
25. Zhang, Y.; Lu, D.; Li, H.; Kondamareddy, K.K.; Wang, H.; Zhang, B.; Wang, J.; Wu, Q.; Zeng, Y.; Zhang, X.; et al. Enhanced visible Light-Driven photocatalytic hydrogen evolution and stability for noble Metal-Free $MoS_2/Zn_{0.5}Cd_{0.5}S$ heterostructures with W/Z phase junctions. *Appl. Surf. Sci.* **2022**, *586*, 152770. [CrossRef]
26. Dong, W.; Cai, T.; Wang, L.; Liu, C.; Chen, H.; Li, W.; Liu, Y.; Xia, X. Optimized removal of antibiotics over $Cd_{0.5}Zn_{0.5}S$/NiCo-LDH: Constructing a homojunctions-heterojunctions composite photocatalyst. *J. Environ. Chem. Eng.* **2022**, *10*, 108624. [CrossRef]
27. Qi, S.; Wang, D.; Zhao, Y.; Xu, H. Core–shell g-C_3N_4@$Zn_{0.5}Cd_{0.5}S$ heterojunction photocatalysts with high photocatalytic activity for the degradation of organic dyes. *J. Mater. Sci. Mater. Electron.* **2019**, *30*, 5284–5296. [CrossRef]
28. Madhusudan, P.; Wageh, S.; Al-Ghamdi, A.A.; Zhang, J.; Cheng, B.; Yu, Y. Graphene-$Zn_{0.5}Cd_{0.5}S$ nanocomposite with enhanced visible-light photocatalytic CO_2 reduction activity. *Appl. Surf. Sci.* **2020**, *506*, 144683. [CrossRef]
29. Qiu, J.; Zhang, X.-F.; Zhang, X.; Feng, Y.; Li, Y.; Yang, L.; Lu, H.; Yao, J. Constructing $Cd_{0.5}Zn_{0.5}S$@ZIF-8 nanocomposites through self-assembly strategy to enhance Cr(VI) photocatalytic reduction. *J. Hazard. Mater.* **2018**, *349*, 234–241. [CrossRef] [PubMed]
30. Wang, X.; Zhang, Y.; Miao, W.; Zhang, X.; Shi, Y.; Tang, Z.; Shi, H. Insight into the pathway, improvement of performance and photocatalytic mechanism of active carbon/$Bi_4O_5Br_2$ composite for cefixime and rhodamine B removal. *J. Photochem. Photobiol. Chem.* **2023**, *444*, 114892. [CrossRef]
31. Zhou, X.; Wu, J.; Xiao, Y.; Jiang, Y.; Zhang, W.; Liu, Y.; Liu, Z.; Zhang, J. Boosting photoelectron transport in $Zn_{0.5}Cd_{0.5}S/Sn_3O_4$ heterostructure through close interface contact for enhancing photocatalytic H_2 generation and degradation of tetracycline hydrochloride. *Sep. Purif. Technol.* **2023**, *311*, 123243. [CrossRef]
32. Xiao, Y.; Jiang, Y.; Zhou, E.; Zhang, W.; Liu, Y.; Zhang, J.; Wu, X.; Qi, Q.; Liu, Z. In-suit fabricating an efficient electronic transport channels via S-scheme polyaniline/$Cd_{0.5}Zn_{0.5}S$ heterojunction for rapid removal of tetracycline hydrochloride and hydrogen production. *J. Mater. Sci. Technol.* **2023**, *153*, 205–218. [CrossRef]
33. Li, A.; Pang, H.; Li, P.; Zhang, N.; Chen, G.; Meng, X.; Liu, M.; Liu, X.; Ma, R.; Ye, J. Insights into the critical dual-effect of acid treatment on $Zn_xCd_{1-x}S$ for enhanced photocatalytic production of syngas under visible light. *Appl. Catal. B Environ.* **2021**, *288*, 119976. [CrossRef]
34. Madhusudan, P.; Shi, R.; Xiang, S.; Jin, M.; Chandrashekar, B.N.; Wang, J.; Wang, W.; Peng, O.; Amini, A.; Cheng, C. Construction of highly efficient Z-scheme $Zn_xCd_{1-x}S$/Au@g-C_3N_4 ternary heterojunction composite for visible-light-driven photocatalytic reduction of CO_2 to solar fuel. *Appl. Catal. B Environ.* **2021**, *282*, 119600. [CrossRef]
35. Cao, W.; Jiang, C.; Chen, C.; Zhou, H.; Wang, Y. A novel Z-scheme CdS/$Bi_4O_5Br_2$ heterostructure with mechanism analysis: Enhanced photocatalytic performance. *J. Alloys Compd.* **2021**, *861*, 158554. [CrossRef]
36. Ye, L.; Jin, X.; Liu, C.; Ding, C.; Xie, H.; Chu, K.H.; Wong, P.K. Thickness-ultrathin and bismuth-rich strategies for BiOBr to enhance photoreduction of CO_2 into solar fuels. *Appl. Catal. B Environ.* **2016**, *187*, 281–290. [CrossRef]
37. Meng, S.; Bi, Y.; Yan, T.; Zhang, Y.; Wu, T.; Shao, Y.; Wei, D.; Du, B. Room-temperature fabrication of bismuth oxybromide/oxyiodide photocatalyst and efficient degradation of phenolic pollutants under visible light. *J. Hazard. Mater.* **2018**, *358*, 20–32. [CrossRef] [PubMed]
38. Cai, M.; Liu, Y.; Wang, C.; Lin, W.; Li, S. Novel $Cd_{0.5}Zn_{0.5}S/Bi_2MoO_6$ S-scheme heterojunction for boosting the photodegradation of antibiotic enrofloxacin: Degradation pathway, mechanism and toxicity assessment. *Sep. Purif. Technol.* **2023**, *304*, 122401. [CrossRef]
39. Xia, D.; Hu, L.; Wang, Y.; Xu, B.; Liao, Y.; He, C.; Ye, L.; Liang, X.; Ye, Y.; Shu, D. Immobilization of facet-engineered Ag_3PO_4 on mesoporous Al_2O_3 for efficient industrial waste gas purification with indoor LED illumination. *Appl. Catal. B Environ.* **2019**, *256*, 117811. [CrossRef]
40. Guo, F.; Huang, X.; Chen, Z.; Ren, H.; Li, M.; Chen, L. MoS_2 nanosheets anchored on porous $ZnSnO_3$ cubes as an efficient visible-light-driven composite photocatalyst for the degradation of tetracycline and mechanism insight. *J. Hazard. Mater.* **2020**, *390*, 122158. [CrossRef]
41. Pei, C.Y.; Chen, Y.G.; Wang, L.; Chen, W.; Huang, G.B. Step-scheme $WO_3/CdIn_2S_4$ hybrid system with high visible light activity for tetracycline hydrochloride photodegradation. *Appl. Surf. Sci.* **2021**, *535*, 147682. [CrossRef]
42. Lai, C.; Zhang, M.; Li, B.; Huang, D.; Zeng, G.; Qin, L.; Liu, X.; Yi, H.; Cheng, M.; Li, L.; et al. Fabrication of CuS/$BiVO_4$ (0 4 0) binary heterojunction photocatalysts with enhanced photocatalytic activity for Ciprofloxacin degradation and mechanism insight. *Chem. Eng. J.* **2019**, *358*, 891–902. [CrossRef]
43. Xu, Y.; You, Y.; Huang, H.; Guo, Y.; Zhang, Y. Bi_4NbO_8Cl {001} nanosheets coupled with g-C_3N_4 as 2D/2D heterojunction for photocatalytic degradation and CO_2 reduction. *J. Hazard. Mater.* **2020**, *381*, 121159. [CrossRef] [PubMed]
44. Xu, Y.; Ma, Y.; Ji, H.; Huang, S.; Xie, M.; Zhao, Y.; Xu, H.; Li, H. Enhanced long-wavelength light utilization with polyaniline/bismuth-rich bismuth oxyhalide composite towards photocatalytic degradation of antibiotics. *J. Colloid Interface Sci.* **2019**, *537*, 101–111. [CrossRef]

45. Shi, Y.; Wang, L.; Dong, S.; Miao, X.; Zhang, M.; Sun, K.; Zhang, Y.; Cao, Z.; Sun, J. Wool-ball-like BiOBr@ZnFe-MOF composites for degradation organic pollutant under visible-light: Synthesis, performance, characterization and mechanism. *Opt. Mater.* **2022**, *131*, 112580. [CrossRef]
46. Luangwanta, T.; Chachvalvutikul, A.; Kaowphong, S. Facile synthesis and enhanced photocatalytic activity of a novel $FeVO_4/Bi_4O_5Br_2$ heterojunction photocatalyst through step-scheme charge transfer mechanism. Colloids Surf. *Physicochem. Eng. Asp.* **2021**, *627*, 127217. [CrossRef]
47. Ma, X.; Chen, K.; Niu, B.; Li, Y.; Wang, L.; Huang, J.; She, H.; Wang, Q. Preparation of $BiOCl_{0.9}I_{0.1}/\beta\text{-}Bi_2O_3$ composite for degradation of tetracycline hydrochloride under simulated sunlight. *Chin. J. Catal.* **2020**, *41*, 1535–1543. [CrossRef]
48. Li, X.; Sun, Y.; Xiong, T.; Jiang, G.; Zhang, Y.; Wu, Z.; Dong, F. Activation of amorphous bismuth oxide via plasmonic Bi metal for efficient visible-light photocatalysis. *J. Catal.* **2017**, *352*, 102–112. [CrossRef]
49. Wang, W.; Li, Z.; Wu, K.; Dai, G.; Chen, Q.; Zhou, L.; Zheng, J.; Ma, L.; Li, G.; Wang, W.; et al. Novel Ag-bridged dual Z-scheme $g\text{-}C_3N_4/BiOI/AgI$ plasmonic heterojunction: Exceptional photocatalytic activity towards tetracycline and the mechanism insight. *J. Environ. Sci.* **2023**, *131*, 123–140. [CrossRef]
50. Fei, Q.; Yin, H.; Yuan, C.; Zhang, Y.; Zhao, Q.; Lv, H.; Zhang, Y.; Zhang, Y. Visible-light-driven $AgI/Bi_4O_5I_2$ S-scheme heterojunction for efficient tetracycline hydrochloride removal: Mechanism and degradation pathway. *Chemosphere* **2023**, *337*, 139326. [CrossRef]
51. Wang, Y.; Xiao, X.; Ding, T.; Lu, M. Mixed 1T-2H phase $MoSe_2$ as interfacial charge-transfer-bridge to boosting photocatalytic activity of dual Z-scheme AgI/1T-2H $MoSe_2/Bi_4O_5Br_2$ heterojunction. *J. Alloys Compd.* **2021**, *875*, 160092. [CrossRef]